Article

Operation of Photo Electron Spectrometers for Non-Invasive Photon Diagnostics at the European X-Ray Free Electron Laser

Joakim Laksman, Florian Dietrich, Theophilos Maltezopoulos, Jia Liu, Danilo Enoque Ferreira de Lima, Natalia Gerasimova, Ivars Karpics, Naresh Kujala, Philipp Schmidt, Suren Karabekyan et al.

Article

Operation of Photo Electron Spectrometers for Non-Invasive Photon Diagnostics at the European X-Ray Free Electron Laser

Joakim Laksman *, **Florian Dietrich**, **Theophilos Maltezopoulos**, **Jia Liu**, **Danilo Enoque Ferreira de Lima**, **Natalia Gerasimova**, **Ivars Karpics**, **Naresh Kujala**, **Philipp Schmidt**, **Suren Karabekyan**, **Svitozar Serkez** and **Jan Grünert**

European X-Ray Free-Electron Laser Facility GmbH, Holzkoppel 4, 22869 Schenefeld, Germany; florian.dietrich@xfel.eu (F.D.); theophilos.maltezopoulos@xfel.eu (T.M.); jia.liu@xfel.eu (J.L.); danilo.enoque.ferreira.de.lima@xfel.eu (D.E.f.d.L.); natalia.gerasimova@xfel.eu (N.G.); ivars.karpics@xfel.eu (I.K.); naresh.kujala@xfel.eu (N.K.); philipp.schmidt@xfel.eu (P.S.); suren.karabekyan@xfel.eu (S.K.); svitozar.serkez@xfel.eu (S.S.); jan.gruenert@xfel.eu (J.G.)
* Correspondence: joakim.laksman@xfel.eu

Abstract: Angle-resolved photoelectron spectrometers with microchannel plate detectors and fast digitizer electronics are versatile and powerful devices for providing non-invasive single-shot photon diagnostics at a MHz repetition rate X-ray free-electron lasers. In this contribution, we demonstrate and characterize the performance of our two operational photoelectron spectrometers for the application of hard X-rays and soft X-rays as well as new automation tools and online data analysis that enable continuous support for machine operators and instrument scientists. Customized software has been developed for the real-time monitoring of photon beam polarization and spectral distribution both in single-color and two-color operation. Hard X-ray operation imposes specific design challenges due to poor photoionization cross-sections and very high photoelectron velocities. Furthermore, recent advancements in machine learning enable resolution enhancement by training the photoelectron spectrometer together with an invasive high-resolution spectrometer, which generates a response function model.

Keywords: photon diagnostics; photoelectron spectrometer; polarimetry; X-ray; free electron laser

1. Introduction

The concept of linear-accelerator-based self-amplification of spontaneous emission (SASE) is that electrons are accelerated to approach the speed of light before being injected into a periodic magnetic field undulator, where electromagnetic radiation is produced. The spatial modulation of electron bunches occurs in an interplay with the electromagnetic field, causing them to radiate in phase and generate coherent and brilliant X-ray pulses. The unique properties of X-ray free-electron laser (XFEL) radiation, including high intensity, high repetition rate, and short pulse length, have found applications in various scientific disciplines and created a demand for the development of instrumentation for photon diagnostics [1–4]. At the European XFEL facility in Schenefeld, Germany, a variety of techniques are used to provide beam parameters to users and operators [5–9]. A non-invasive principle for photon diagnostics involves using a low-density matter target that is ionized by XFEL pulses with the resulting ions or electrons encoding information about the single-shot characteristics. A gas-based device that provides machine operators and users with pulse-resolved information is the photoelectron spectrometer (PES), which measures spectral distribution and polarization. Gas target selection takes into consideration the electron binding energy (E_B), the lifetime broadening (Γ), the photoionization cross-section (σ), and the anisotropy parameter (β) [10–15]. Two conceptually different spectrometers have been developed and commissioned at European XFEL with their respective designs influenced by user requirements and beam conditions:

1. The hard X-ray PES (hxPES) performance was tested and characterized at the hard X-ray synchrotron PETRA III, P09 beamline [16]. After that, it was commissioned in early 2022 at the SASE1 beamline with the downstream scientific instruments *Single Particles, Clusters, and Biomolecules & Serial Femtosecond Crystallography*(SPB/SFX) [17] and *Femtosecond X-ray Experiments* (FXE) [18]. Typical applications include experiments at resonances where narrow and precise bandwidth is crucial as well as absolute photon energy calibration. The monochromator is used to select the desired photon energy, but users rely on precise undulator tuning, which can only be achieved with the non-invasive diagnostics that the PES provides. The design of the hxPES had to account for very high electron kinetic energies, requiring a robust construction for an applied voltage of up to 10 kV without dielectric breakdown. Moreover, the poor photoionization cross-section places stringent demands on electron optics for high detection efficiency.

2. The soft X-ray PES (sxPES) [19] in operation since the beginning of 2018 supports the SASE3 beamline with the instruments *Small Quantum Systems* (SQS) and *Spectroscopy and Coherent Scattering* (SCS) as well as the recently commissioned *Soft X-ray Port* (SXP). Experiments where the undulator gap is tuned to scan the photon energy require reliable and well-calibrated spectral distribution diagnostics over the entire range [20]. For studies of X-ray magnetic circular dichroism, circular birefringence and chirality [21,22], the beamline offers arbitrary elliptical polarization [23]. Polarization diagnostics requires angle-resolved spectroscopy, which is achieved with a total of 16 detectors distributed along the polar angle. Furthermore, two-color operation with an optical delay for pump–probe studies demands independent control of retardation voltages for individual flight-tubes [24].

In this research paper, we report on the commissioning of the new hxPES in SASE1 and on the recent progress and new available features with our sxPES in SASE3. We describe software developments that enable automatic operation and online data analysis, providing reliable photon diagnostics to machine operators and instruments.

2. Instrument

The operation principle of the PES is that atoms in a low-density matter target are ionized whereupon photoelectrons are emitted with a kinetic energy (E_K) that is proportional to the photon energy ($\hbar\omega$) according to the photoelectric effect, $E_K = \hbar\omega - E_B$ where E_B, is the binding energy of the electron before its emission. Flight tubes with an applied retardation voltage act as dispersive elements where the time is measured from the instant of ionization until electrons reach a microchannel plate-based detector. Data acquisition is performed with digitizer boards (Teledyne SP Devices ADQ 412-4G) in a μTCA crate. The boards can be operated either in four-channel mode with $2\,\text{GSs}^{-1}$ ($0.5\,\text{ns}$ binning), or optionally, two channels can be bridged in order to increase the sample rate to $4\,\text{GSs}^{-1}$ ($0.25\,\text{ns}$ binning). The dynamic range is $\pm 400\,\text{mV}$. A fluxgate-type magnetometer is mounted near the source region. A three-axis Helmholtz coil structure surrounds the device to compensate for the background magnetic field, which would otherwise affect the electron trajectories. The design was imported into the commercial software *Simion 8.2* to optimize the collection efficiency and resolving power for a range of electron kinetic energies spanning several keV [25]. Figure 1 shows simulated electron trajectories for (a) sxPES and (b) hxPES.
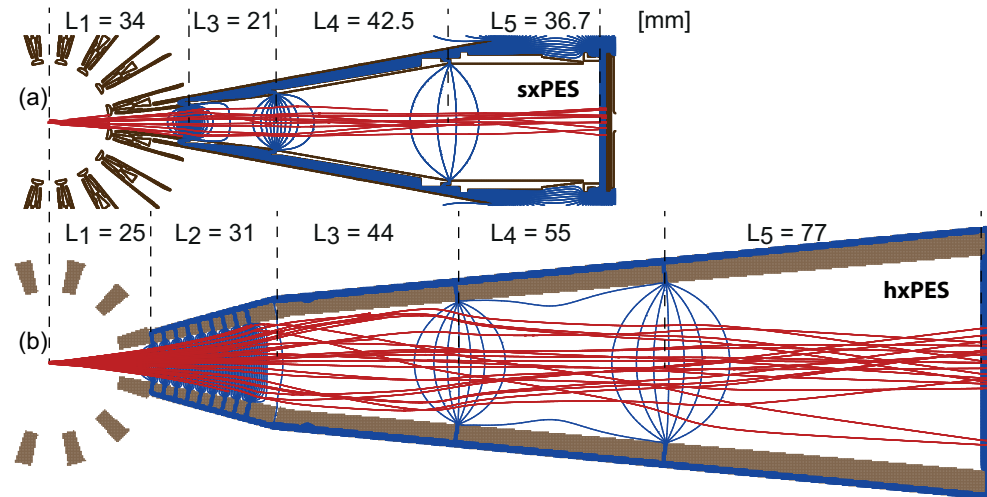
Figure 1. Cross-section of flight tubes with simulated electron trajectories (red lines) for sxPES (**a**) and hxPES (**b**). Potential gradients are indicated with blue contours.

In the hxPES, generally, the flight tube segments can be modeled as field free regions when not considering field penetration. An exception is the second segment, which is a retardation region designed to dramatically reduce the electron kinetic energy. In a non-relativistic treatment, the spectral distribution of each pulse is encoded in the time of flight (TOF) according to the analytical expression

$$T_n = \frac{L_n}{v_n} \tag{1}$$

for $n \in 1, 3, 4, 5$, where L_n and v_n are the flight-tube length and velocity in region n. v_n is given by E_K and the applied voltage V_n,

$$v_n = \sqrt{\frac{2 \cdot e^- \cdot (E_K - c_n \cdot V_n)}{m_e}}. \tag{2}$$

c_n are correction factors—typically very close to 1—that take into account field penetration between segments. They are found for each segment by comparing with electron trajectory simulations and, if the fixed voltage ratio is kept, are valid for a large voltage range. In addition to field free regions, the second stage ($n = 2$) is a retardation region with a constant electric field. The acceleration of an electron is given by the Lorentz force, that in the absence of magnetic fields is $\vec{a} = \frac{e^-}{m_e} \cdot \vec{\nabla} V$, which leads to retardation, velocity and distance traveled as a function of time

$$a_2 = \frac{e^-}{m_e} \cdot \frac{c_2 \cdot V_2 - c_1 \cdot V_1}{L_2} \tag{3}$$

$$v_2(t) = a_2 \cdot t + v_1, \tag{4}$$

$$x_2(t) = \frac{a_2}{2} \cdot t^2 + v_1 \cdot t \tag{5}$$

At the end of the retardation region, we have the relation $x_2(T_2) \equiv L_2$; thus, the time an electron spends in the retardation region is

$$T_2 = \frac{-v_1 + \sqrt{v_1^2 + 2 \cdot L_2 \cdot a_2}}{a_2}. \tag{6}$$

The total TOF is

$$T = \sum_{n=1}^{5} T_n \tag{7}$$

which applies also to sxPES, although there, the retardation region must be omitted ($L_2 = 0$). Inverting the relation to derive $E_K(T)$ analytically, which is necessary for calibration, is complicated. Therefore, we employ numerical methods that continuously update the inversion in real time while the retardation voltages are being tuned, ensuring that reliable spectral distribution is provided without relying on libraries of computer-simulated calibrations.

Auger–Meitner transitions occur at fixed electron kinetic energies, providing features suitable for testing the validity of the calibration. For Krypton, LMM and LMN lines are well established from a range of experimental studies [26–30]. Figure 2a shows calibrated spectra from L_1, L_2, and L_3 Auger transitions taken with hxPES at different retardation voltages, which were each selected to focus on a particular kinetic energy region. Eight bands, labeled A–H, are identified. Note that for a fixed retardation voltage, resolution increases with decreasing kinetic energy. Transitions that are monitored at several retardation voltages are better resolved for higher retardation (temporal dispersion). The photon energy of 12 keV is below the K-shell ionization and was selected to prevent corresponding Auger cascades from contributing energy levels. The detector at 90° was used where direct photoionization lines are suppressed due to the horizontal polarization of the X-rays. The digitizer was configured to the highest available sampling rate of $4\,\mathrm{GSs}^{-1}$. Enlarged regions of the spectra are presented in Figure 2b–f for comparison with literature data. Each transition leads to several final states, whereof the kinetic energies of the dominating states have been marked with vertical dashed lines in each panel. High agreement is found. We can confidently assign the Auger–Meitner transitions, and we estimate a calibration error of <5 eV. In particular, at the retardation voltage 1490 V and the transition $L_2M_{4,5}M_{4,5}$, the $^1S_0$ (1504.9 eV) and $^1G_4$ (1512.7 eV) final states are resolved. Thus, at around 1500 eV kinetic energy, a resolution of better than 8 eV is demonstrated. For hxPES, in addition to Krypton Auger–Meitner transitions, also Argon KLL and KLM [31] as well as Xenon LMM and LMN [32] lines were successfully used with this approach to validate the calibration. For sxPES, Neon KLL [33] and N_2 KVV [34,35] transitions were used.

Flight tubes are distributed in a plane oriented perpendicular with respect to the X-ray beam [19]. Recording signal intensity over the polar angle (θ) allows for polarization measurements. For the fixed azimuth angle $\phi = 0°$, the polarization function $P(\theta)$ describes the photoemission intensity as a function of θ [1],

$$P(\theta) = 1 + \frac{\beta}{4}\left(1 + 3 \cdot P_L \cos\left(2(\theta - \psi)\right)\right). \tag{8}$$

P_L is the linear polarization component and ψ is the tilt angle. Assuming no unpolarized contribution, the degree of circular polarization is given as $P_C = \sqrt{1 - P_L^2}$. For perfect horizontal polarization, $P_L = 1$ and $\psi = 0$. β is the anisotropy parameter of the target gas electronic configuration and depends on the photon energy.
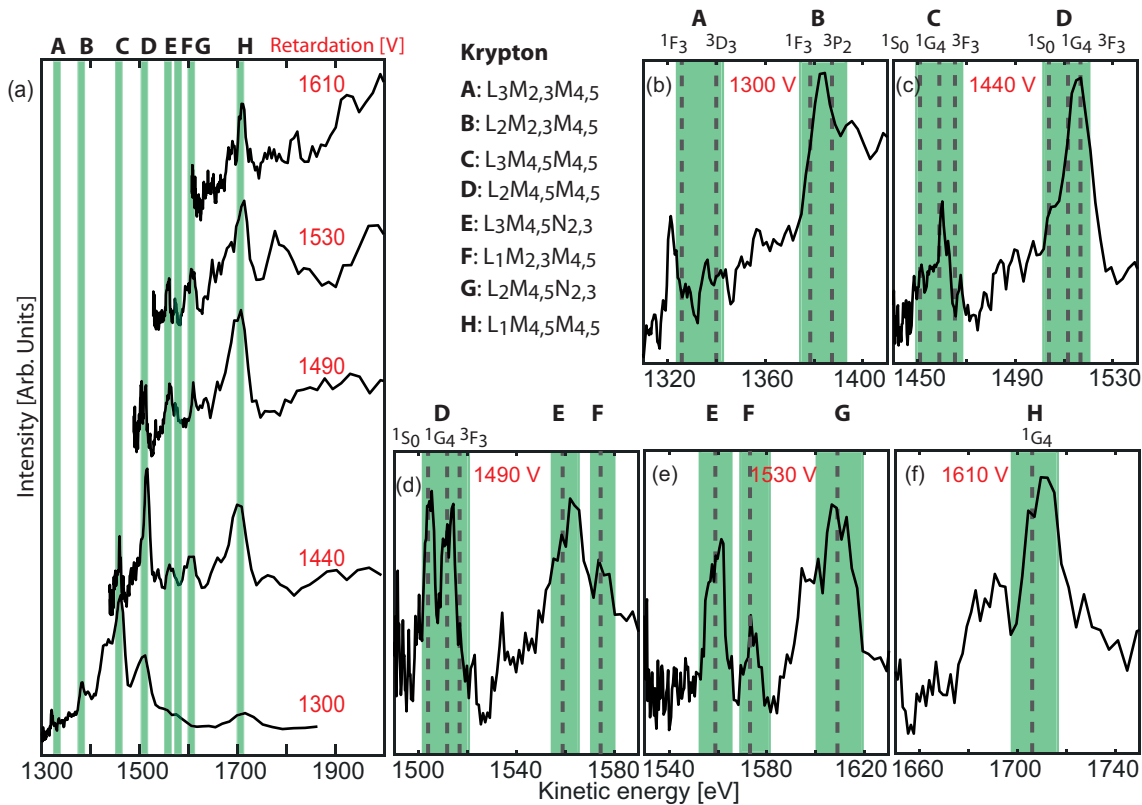
Figure 2. (**a**) Krypton LMM and LMN Auger–Meitner lines measured with hxPES at $\hbar\omega = 12\,\text{keV}$. Retardation voltage was tuned in the range 1300 to 1610 V. The detector at 90° was used, and the digitizer was configured to $4\,\text{GSs}^{-1}$. The conversion to kinetic energy is made for each retardation voltage and is based on numerical inversion of the analytical calibration using Equations (1)–(7). Panels (**b**–**f**) show expanded views of each band A–H. Dashed lines indicate final states.

3. Hard X-Rays

Figure 3 shows single-pulse spectra of Xenon $2p_{3/2}$ measured with the hxPES [16] at the SASE1 beamline. The undulator gap was tuned for 9450 eV radiation. Binding energy is $E_B = 4786.47\,\text{eV}$ [13] and natural line broadening is $\Gamma = 2.60\,\text{eV}$ [36]. At this photon energy, the anisotropy parameter is $\beta \approx 1.47$ [14] and the photoionization cross-section is $\sigma \approx 0.04\,\text{Mb}$ [11]. Although the spectrometer has 12 flight tubes, it was equipped with only four detectors during these measurements. Now, two additional detectors have been assembled and installed on the device to improve the signal statistics. Figure 3a presents electron TOF spectra from one single photon pulse recorded with the four available detectors. The signal from scattered light defines a prompt that represents the instant of ionization subtracted by 0.83 ns due to the time it takes photons to reach the detectors. The peaks in region 5 ns–15 ns are related to valence photoelectrons and Auger–Meitner electrons where the high kinetic energy leads to short TOF. Around 30 ns, we see the Xe $2p_{3/2}$ photoelectrons that have been decelerated from very high kinetic energies, around 4660 eV, to only a few 10 eV. The retardation voltage was set to −4630 V. Figure 3b shows the Xe $2p_{3/2}$ spectra converted from TOF to spectral distribution according to our calibration function. The gray area plot shows the spectral distribution for an average of 100 pulses. As is expected from the polarization function, Equation (8), for linear horizontal polarization and a positive anisotropy parameter, the intensity reaches a maximum at 0° and 180°, and is decreased at 150°. The detector located at 90° provides only a minor contribution to the total intensity. The challenge in the hard X-ray regime, for single-pulse photon diagnostics, is the poor photoionization cross-section with the consequence that one detector alone does not provide sufficient statistics to represent the actual spectral distribution, and thus it is needed to combine the signals from several detectors. Figure 3c

shows the sum of the four detectors (red line). As a means to validate the reliability of the photoelectron spectrum and of the calibration, we compare with a spectrum measured for the same photon pulse by the downstream located HIREX (HIgh REsolution hard X-ray) spectrometer [7]. This is a single-shot spectrometer, based on a bent crystal as a dispersive element, and a MHz-repetition rate strip detector. Optionally, an upstream diamond diffraction grating can be used in transmission to split off a small fraction (0.1%) of the photon beam for this analysis instead of using the zero-order direct beam which is propagated to and used at the experiment endstation. The HIREX and the hxPES are two complementary and independently calibrated devices for spectral diagnostics. At 9 keV, the HIREX offers a high spectral resolution of about 0.3 eV, but in contrast to the PES, it is partially invasive and has a measurement rate of 0.5 MHz limited by the currently used Gotthard-I detector, whereas the PES can provide diagnostics up to the maximum repetition rate of 4.5 MHz available at European XFEL. Figure 3d shows five subsequent single-shot photon pulses measured with both the PES and the HIREX.
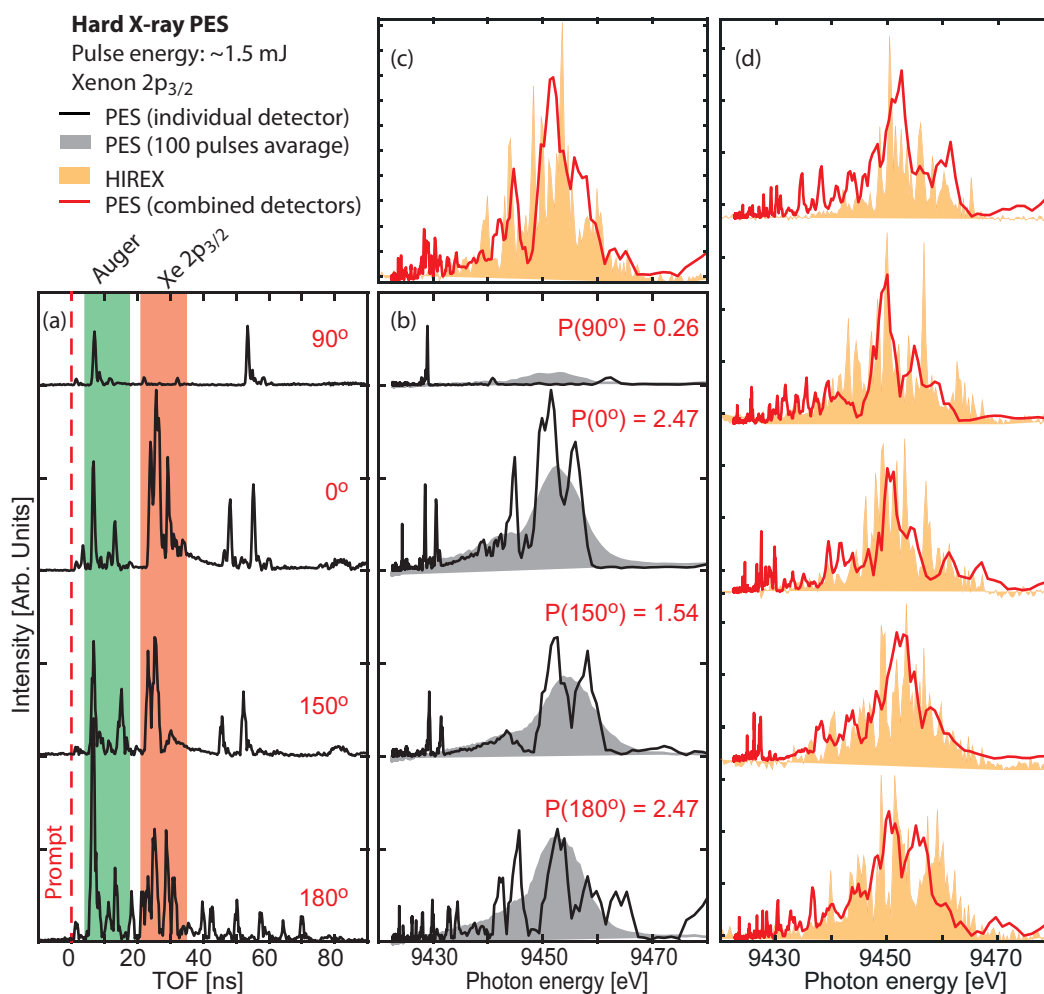

Figure 3. Single pulse at 9450 eV. (**a**) TOF spectra for the same pulse recorded on detectors in four different orientations. Retardation is -4630 V. (**b**) Single-shot Xe $2p_{3/2}$ peak transformed from TOF to photon energy (black line). Average of 100 pulses (gray area). (**c**) Sum of spectra from all four detectors (red line). Same pulse detected on HIREX (orange area). (**d**) Five typical single-shot photon pulses measured with both the hxPES and the HIREX.

4. Soft X-Rays: Polarization

The regular planar undulators at the European XFEL contain permanent neodymium magnets arranged to generate linearly polarized radiation with the polarization axis in the

horizontal plane. To obtain variable polarization in the soft X-ray regime, an afterburner consisting of four APPLE-X helical undulators was implemented behind the SASE3 planar undulator system [23]. The sxPES supported the commissioning of the afterburner with online polarization photon diagnostics. Figure 4a–c shows the TOF spectra for Neon 1s a few dozen eV above the resonance on eight detectors in different orientations with respect to the polarization vector of light for three different polarization configurations. The binding energy (E_B) is 870.2 eV and the natural line width is $\Gamma = 0.24$ eV. The Ne 1s photoionization cross-section at this photon energy range is $\sigma > 0.2$ Mb, and the anistropy parameter is $\beta = 2$ [10,12]. The pulse energy is about 100 µJ. We have averaged 20 pulses for each spectrum to improve the signal-to-noise ratio. The retardation voltage is fixed at 6 V. The angle-resolved measurement with the undulator tuned to 900 eV at horizontal linear polarization is presented in Figure 4a. The distribution is anisotropic with the Ne 1s peak intensity close to zero at 90°. The intensity increases as a function of the angle and reaches its maximum at 0°. Figure 4b shows the angle-resolved spectra for 885 eV at vertical linear polarization, where the intensity is maximum at 90° and vanishes at 0°. The wider TOF distribution for vertical polarization compared to horizontal polarization is related to the lower photon energy and subsequent lower electron kinetic energy, which corresponds to a longer TOF and a broader distribution. Figure 4c presents the spectra for circular polarization at 890 eV where angular dependence is isotropic.
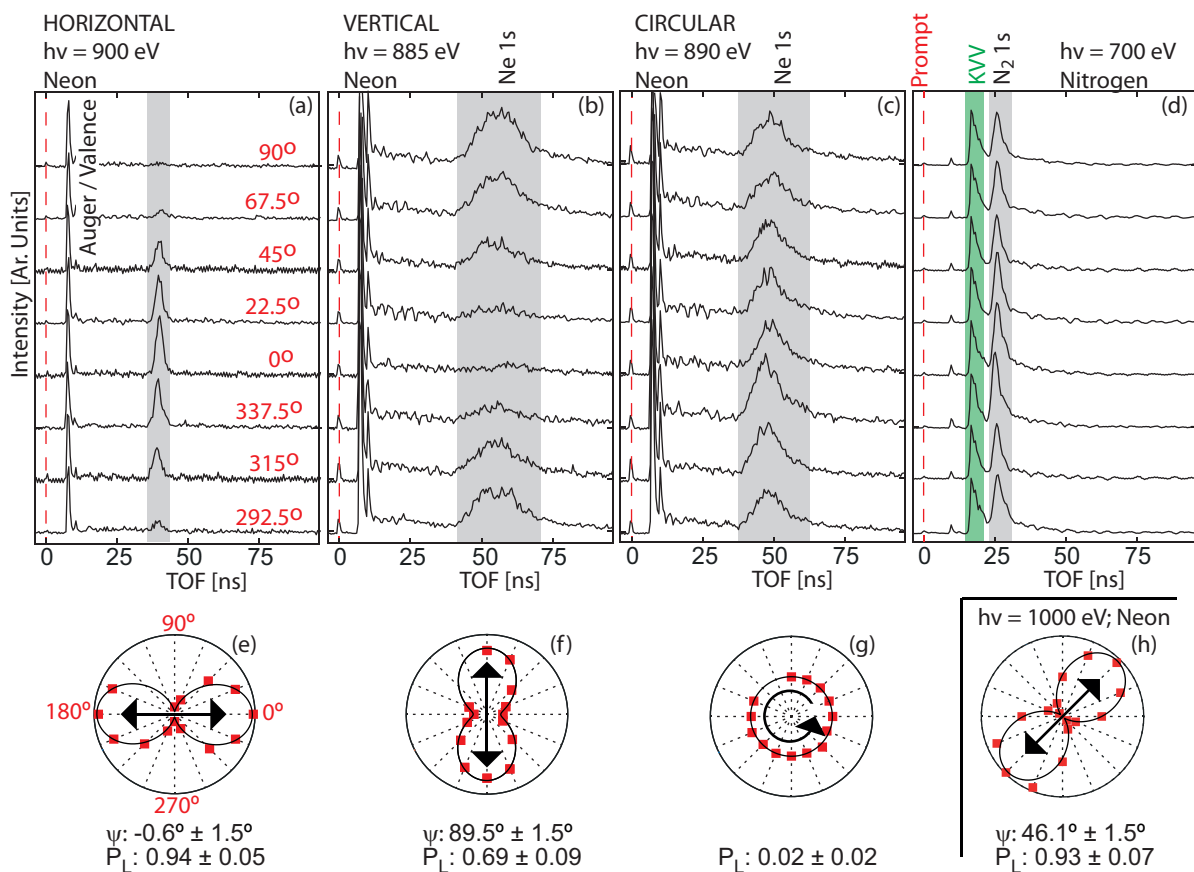

Figure 4. The intensity of electron TOF spectra with sxPES displays angular dependence for different settings of the helical undulator: horizontal (**a**), vertical (**b**) and circular polarization (**c**). (**d**) N₂ KVV lines are used for detector signal normalization. (**e–g**) Angular intensity distribution is presented in polar plots with 14 detectors active. Fitting with Equation (8) gives us the degree of linear polarization and the tilt angle. (**h**) Angular distribution with helical undulator set to +45° at 1000 eV taken at a different occasion with all 16 detectors active.

The detector and flight-tube performance is not identical; thus, the peak intensity must be normalized, which is accomplished with Auger–Meitner lines whose polar and azimuth intensity distribution is nearly isotropic. In particular, the N_2 KVV transition energies in the range 357 eV to 367 eV are useful for this purpose [37]. Figure 4d presents electron TOF data for eight of the detectors from an N_2 target at $\hbar\omega = 700$ eV with -261 V retardation voltage. The data are averaged over 20 pulses for reliable statistics. The intensity of the KVV peak at about 17 ns (shaded green area) is used to normalize the detector performance by calculating a calibration factor for each detector. In addition to the Auger–Meitner band, the N_2 1s peak ($\beta = 2$) is seen at about 27 ns. These data were collected with the helical undulator tuned to elliptical polarization, thus explaining the almost isotropic distribution of N_2 1s photoelectrons. During this study, 14 out of the total 16 detectors were used. The intensity normalized Ne 1s peak in Figure 4a–c is integrated over the gray area and presented in polar coordinates in Figure 4e–g. Figure 4h shows the angular distribution with the helical undulator set to $+45°$ at 1000 eV taken at a different occasion with all 16 detectors active. The polarization function in Equation (8) was fitted to the data points from which we can extract P_L and ψ.

Observe that this technique is insensitive to whether the non-linear contribution is from unpolarized or right-hand or left-hand polarization in contrast to invasive multilayer-based polarimetry where the complete Stokes vector is measured [1,38].

5. Soft X-Rays: Two Color Operation

X-ray pump/X-ray probe applications are made possible at the European XFEL SASE3 beamline by generating two X-ray pulses with different photon energies. The controllable temporal delay is enabled by a magnetic chicane and in the future also by an optical delay line, which is an ongoing upgrade project to be implemented between the two undulator sections of cell 2–12 (U1) and cell 14–23 (U2) A schematic for the hardware configuration for two-color operation is depicted in Figure 5a. The measured spectral distribution for single bunches where the same electron bunch is lasing first at 945 eV in U1 and subsequently at 905 eV in U2 is displayed in Figure 5b. The target gas is neon. The flight-tube retardation voltages for the sxPES are individually controlled, and thus we can independently select one group for a certain photon energy and another group for the other photon energy. Detectors at 157.5°, 180° and 202.5° (blue) are tuned to -60 V to achieve optimal resolving power for the 945 eV spectrum. Detectors at 22.5°, 0° and 337.5° (red) are tuned to -20 V to achieve optimal resolving power for the 905 eV spectrum. Drift tubes on the horizontal plane are selected to take advantage of the higher yield due to the horizontal polarization of the X-rays and the positive β value of the Ne 1s photo line. Figure 5b shows four typical subsequent single-shot spectra where we combined the intensity from three detectors for each color. Flight tubes set to the higher retardation voltage discriminate against photoelectrons emitted by the lower photon energy pulse (blue line). The lower retardation voltage has as a consequence that also the Ne 1s peak emitted from the 945 eV pulse is included in the spectra but with lower spectral resolution (red line). This data set was collected together with the invasive high-resolution grating spectrometer (GS) (black line) [9] to enable us to confirm the PES calibration and also to verify that the PES spectra are representative of the actual spectral distribution.

Furthermore, two-color operation invalidates information from the X-ray Gas Monitor (XGM) which can only deliver absolutely calibrated pulse energy data for pulses with a single photon energy [6]. Therefore, in addition to spectral and polarization characterization, pulse energy diagnostics also becomes the responsibility of the sxPES during two-color operation. The routine is to first produce lasing only with U1 segments and to correlate the pulse energy measured by the XGM with the peak intensity of the PES for that particular setting. The procedure is then repeated for U2. When two-color operation is activated and after preparing with the described calibrations, the pulse energy determination then relies solely on the PES for both colors [24]. Clearly, Figure 5 shows that not only the spectral distribution changes over the trains, but also the intensity ratio varies dramatically.
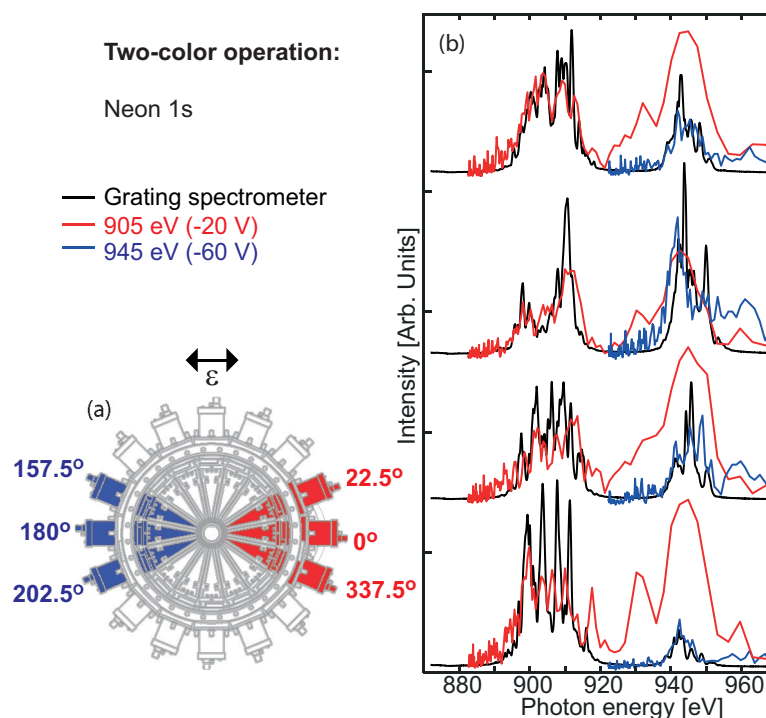
Figure 5. sxPES two-color operation with Ne 1s. (**a**) Flight tubes at 157.5°, 180° and 202.5° are set to −60 V for higher photon energy. Flight tubes at 22.5°, 0° and 337.5° are set to −20 V for lower photon energy. $\vec{\varepsilon}$ indicates the polarization vector. (**b**) Sum of single pulse spectral distribution registered at the two detector groups with undulator sections tuned to 945 eV and 905 eV, respectively. This data set was collected in single-bunch mode, which enables us to compare the spectra with the GS for both colors.

6. Soft X-Rays: Virtual Spectrometer

The limiting factors concerning the spectral resolution of the PES are the natural linewidth of the target gas and the instrumental broadening of the flight tubes that increases with higher electron kinetic energy. This constraint can be circumvented by using the correlation between the gas-based online diagnostics and the GS measurements as was shown in the proof-of-principle study in ref. [8]. The concept is to collect data simultaneously from the GS and the PES previous to the experiment and perform a fit using a regression model to infer the GS only from the pulse-resolved data. After the fit, a model may be used to obtain a higher-quality spectrum from the PES non-invasively at MHz repetition rates. However, such an idea involves a significant amount of data analysis, and it is hard to automate for operations. Developments have been made using further mathematical techniques to automate and streamline the procedure, including full-resolution characterization using European XFEL data under several beam conditions. The final system has been named the Virtual Spectrometer (VS) and has been deployed in a European XFEL control environment [39]. Ref. [40] describes the VS, which includes the online estimate of the resolution, uncertainties, as well as continuous data quality checks. Additionally, the VS avoids the need for a separate calibration of the PES. Figure 6a presents one single-pulse TOF spectrum for the Ne 1s photoelectron at about 1000 eV for six detectors with a digitizer configured to 2 GSs^{-1}. The photoelectron kinetic energy is about 130 eV. The calibration function converts the scale from TOF to photon energy. Indeed, the plots in Figure 6b are each meant to represent the spectral distribution of the same pulse. The discrepancies between the detectors can be attributed to non-identical components for signal electronics that contribute to electronic noise and imperfections in flight tube geometry that can lead to non-uniform detection efficiency. The VS model takes advantage of the wealth of information from all available detectors and reconstructs the spectrum with high fidelity to the actual spectral distribution as is seen in Figure 6c (red line), including

the energy calibration. In addition to TOF data from the digitizers, the model also uses the single-shot pulse-energy data provided by the XGM, which is helpful extra information for the model to take into account non-linear dependence on pulse energy. The reconstructed spectrum is based on a total of 12 detectors, whereof 6 are presented. Comparison with the GS (green dashed line) convolved with a Gaussian distribution of width given by the estimated resolution of the VS for that pulse (full width half maximum 0.91 eV), which was not included in the training data set, demonstrates the validity and reliability of the method. Four spikes with <2 eV separation are clearly resolved that cannot be discerned from only the PES data. The uncertainty band, that is based only on noise and is not related to the resolution, corresponds to a 68 % confidence level. Systematic resolution studies have been performed in ref. [40], demonstrating significantly improved resolution obtained with the VS compared with traditional calibration. Typical single-pulse spectral distributions reconstructed with VS are presented in Figure 6d where the blue dashed line is the actual grating spectra that has not been smeared out via convolution. Although individual spikes cannot be reconstructed by the VS, the main features are clearly seen with intermediate resolution.
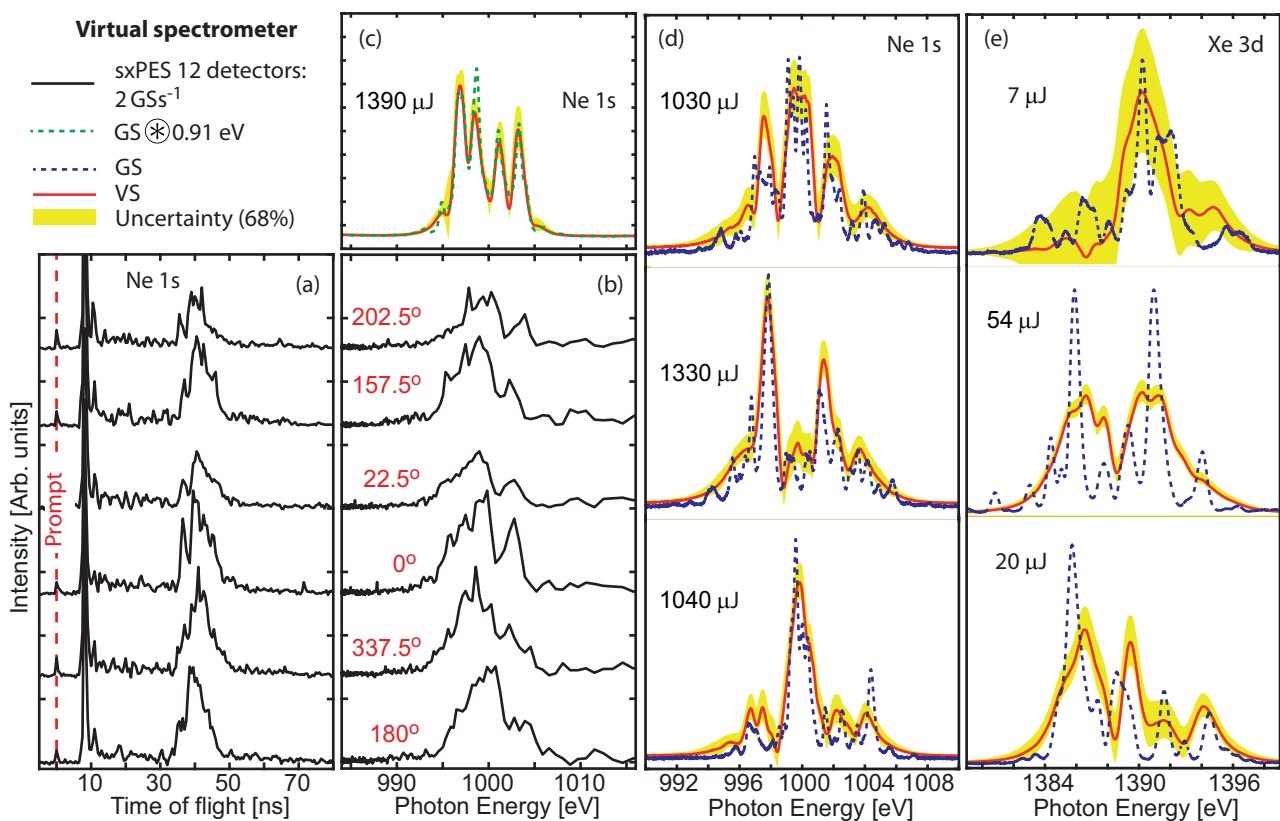

Figure 6. (**a**) TOF spectra with sxPES for Ne 1s from one single pulse registered on several detectors with 2 GSs^{-1}. (**b**) Same spectra calibrated to photon energy. (**c**) Same photon pulse with VS (red line). Four spikes are clearly resolved that cannot be discerned from the raw data. The uncertainty band, that comes from the noise, corresponds to a 68 % confidence level. Comparison with GS convolved with the estimated instrumental linebroadening (green dashed line) demonstrates the validity of the method. (**d**) Examples of typical single-pulse spectral distributions for Ne 1s collected with the VS and compared with non-convolved GS validation data (blue dashed line). (**e**) Examples at the challenging condition of very low pulse energies with Xe 3d target around $\hbar\omega = 1390$ eV.

For very low pulse energies, increasing the operating gas pressure is limited due to HV sparking. When selecting the target gas, the main criteria becomes to maximize the photoionization cross-section. Nonetheless, a poor signal-to-noise ratio makes data

interpretation difficult and thus motivates the use of machine learning. Figure 6e shows three VS single-shot spectra at around 1390 eV acquired with Xe 3d ($\sigma = 0.61$ Mb) [12]. The spin-orbit splitting $3d_{3/2}$ ($E_B = 689.0$ eV, $\Gamma = 490$ meV) and $3d_{5/2}$ ($E_B = 676.4$ eV, $\Gamma = 510$ meV) [15] is sufficiently large to avoid overlap at the typical spectral bandwidth < 12 eV. The flight-tube retardation voltages were selected to include both spin-orbit lines, thus demonstrating that the VS by default takes advantage of all available information. Despite the low pulse energies (<60 μJ) that lead to a poor signal-to-noise ratio in the raw data, and high kinetic energy (>700 eV) that leads to lower instrumental resolution, the reconstruction is still reliable when compared with the validation spectrum (blue dashed line). Under these conditions, we estimate a resolution of 2.3 eV full width half maximum for the reconstructed spectra.

Another benefit of the VS is the situation when Auger–Meitner lines overlap the photoelectron spectra. This is, for example, the case around 770 eV when nitrogen 1s ($E_B = 410.0$ eV overlaps with the nitrogen KVV band at around 360 eV. Normally, photon diagnostics is prevented under these conditions, but the VS automatically removes these features as part of the background subtraction. The virtual spectrometer has the limitation that it assumes that the PES and XGM configurations remain stable throughout the measurements, which imposes a boundary on the ranges of photon energies to be measured before refitting the model by re-inserting the GS. Such a limitation could be removed by establishing a large database of PES and GS conditions and interpolating between them as necessary. This planned development requires a large data-taking campaign covering several photon energies, beam intensities, and related PES configurations. While such a task would be time-consuming, it is technically feasible. More complex regression models may be used to further enhance the capabilities of the system in such conditions. Furthermore, considering that the PES resolving power varies non-linearly over the spectral bandwidth, a future operation mode with VS that we are exploring is to optimize each of the flight-tube retardation voltages to cover a separate photon energy region, thus improving the resolution further. Finally, we plan to implement the VS also for hard X-rays where the training would be performed with hxPES and the HIREX spectrometer [7].

7. Online Monitoring and Automation

One application of the PES is to provide instant feedback to operators regarding lasing performance and spectral characteristics during machine tuning. To make this possible, dedicated automation and monitoring software has been developed at European XFEL: a Karabo device which can be bridged to other environments such as the accelerator control system DOOCS. When the undulator gap changes, the retardation voltages are automatically adjusted to retain the photoelectron peak in a fixed TOF region where the resolving power is optimized. The presented spectral distribution is calibrated with Equations (1)–(7) that continuously update to adjust for changing applied voltages. In two color mode, this is performed for both colors independently. This software device has been deployed for both existing online gas-based spectrometers, the SASE1 PES and the SASE3 PES.

The device also provides online polarimetry diagnostics by fitting the peak intensity from each of the detectors to Equation (8) and presenting the fitting parameters P_L and ψ. In the case of polarimetry, s-orbitals ($\beta = 2$) are preferable since higher anisotropy means more accurate fitting. In photon energy regions where s-orbitals are unavailable for reasons such as very poor σ or overlap with Auger–Meitner lines, p- or d-orbitals must be used where β varies with photon energy. This is in particular relevant below N_2 1s at 410 eV. To perform polarimetry in those regions, while tuning the undulator, the monitoring software device must continuously update the anisotropy parameter from a library file by using feedback from the target gas and the calibrated photon energy. Figure 7 presents the DOOCS panel for online polarization monitoring averaged over 10 pulses for better statistics. The target gas is Krypton and the selected photoemission line is Kr 3d. $\hbar\omega = 402.5$ eV corresponds to $\beta = 1.079$ [12]. Pink bars indicate the integrated intensity over each of the 16 detectors.

The green curve is the fitted Equation (8). Polarization is linear horizontal, and fitting gives $P_L = 0.98 \pm 0.02$ and $\psi = -0.1° \pm 0.9°$.
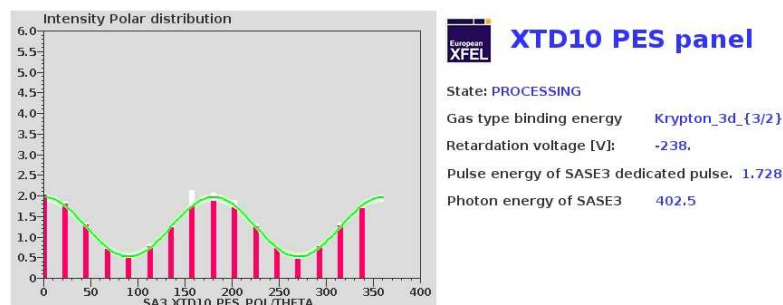

Figure 7. DOOCS panel for online polarization monitoring. The target gas is krypton, and the selected photoemission line is Kr 3d. Pink bars indicate the integrated intensity over each of the 16 detectors. The green curve is the fitted Equation (8). Polarization is linear horizontal.

8. Conclusions

We have provided an overview of the capabilities and operation modes with our versatile photoelectron spectrometers sxPES and hxPES. Auger–Meitner lines have been used to demonstrate the resolving power of the instrument and for calibrations. Software devices have been developed and are continuously being improved with additional features for automation and to provide users and machine operators with online spectral distribution and polarimetry. The scientific impact is that pulse-resolved spectral information enables more detailed data analysis from user experiments. An additional important application that demands non-invasive photon diagnostics is that the online spectra provided by the PES can be used as a veto input for detectors to avoid recording data with undesirable spectral characteristics.

References

1. Allaria, E.; Diviacco, B.; Callegari, C.; Finetti, P.; Mahieu, B.; Viefhaus, J.; Zangrando, M.; De Ninno, G.; Lambert, G.; Ferrari, E.; et al. Control of the Polarization of a Vacuum-Ultraviolet, High-Gain, Free-Electron Laser. *Phys. Rev. X* **2014**, *4*, 041040. [CrossRef]
2. Hartmann, G.; Lindahl, A.O.; Knie, A.; Hartmann, N.; Lutman, A.A.; MacArthur, J.P.; Shevchuk, I.; Buck, J.; Galler, A.; Glownia, J.M.; et al. Circular dichroism measurements at an x-ray free-electron laser with polarization control. *Rev. Sci. Instrum.* **2016**, *87*, 083113. [CrossRef]
3. Bostedt, C.; Boutet, S.; Fritz, D.M.; Huang, Z.; Lee, H.J.; Lemke, H.T.; Robert, A.; Schlotter, W.F.; Turner, J.J.; Williams, G.J. Linac Coherent Light Source: The first five years. *Rev. Mod. Phys.* **2016**, *88*, 015007. [CrossRef]
4. Walter, P.; Kamalov, A.; Gatton, A.; Driver, T.; Bhogadi, D.; Castagna, J.-C.; Cheng, X.; Shi, H.; Obaid, R.; Cryan, J.; et al. Multi-resolution electron spectrometer array for future free-electron laser experiments. *J. Synchrotron Radiat.* **2021**, *28*, 1364–1376. [CrossRef] [PubMed]
5. Grünert, J.; Carbonell, M.P.; Dietrich, F.; Falk, T.; Freund, W.; Koch, A.; Kujala, N.; Laksman, J.; Liu, J.; Maltezopoulos, T.; et al. X-ray photon diagnostics at the European XFEL. *J. Synchrotron Radiat.* **2019**, *26*, 1422–1431. [CrossRef]
6. Sorokin, A.A.; Bican, Y.; Bonfigt, S.; Brachmanski, M.; Braune, M.; Jastrow, U.F.; Gottwald, A.; Kaser, H.; Richter, M.; Tiedtke, K. An X-ray gas monitor for free-electron lasers. *J. Synchrotron Radiat.* **2019**, *26*, 1092–1100. [CrossRef] [PubMed]
7. Kujala, N.; Freund, W.; Liu, J.; Koch, A.; Falk, T.; Planas, M.; Dietrich, F.; Laksman, J.; Maltezopoulos, T.; Risch, J.; et al. Hard x-ray single-shot spectrometer at the European X-ray Free-Electron Laser. *Rev. Sci. Instrum.* **2020**, *91*, 103101. [CrossRef] [PubMed]
8. Li, K.; Laksman, J.; Mazza, T.; Doumy, G.; Koulentianos, D.; Picchiotti, A.; Serkez, S.; Rohringer, N.; Ilchen, M.; Meyer, M.; et al. Ghost-imaging-enhanced noninvasive spectral characterization of stochastic x-ray free-electron-laser pulses. *Commun. Phys.* **2022**, *5*, 191. [CrossRef]
9. Gerasimova, N.; La Civita, D.; Samoylova, L.; Vannoni, M.; Villanueva, R.; Hickin, D.; Carley, R.; Gort, R.; Van Kuiken, B.E.; Miedema, P.; et al. The soft X-ray monochromator at the SASE3 beamline of the European XFEL: From design to operation. *J. Synchrotron Radiat.* **2022**, *29*, 1299–1308. [CrossRef]
10. Krause, M.O.; Oliver, J.H. Natural widths of atomic K and L levels, Kα X-ray lines and several KLL Auger lines. *J. Phys. Chem. Ref. Data* **1979**, *8*, 329–338. [CrossRef]
11. Saloman, E.; Hubbell, J.; Scofield, J. X-ray attenuation cross sections for energies 100 eV to 100 keV and elements Z = 1 to Z = 92. *At. Data Nucl. Data Tables* **1988**, *38*, 1–196. [CrossRef]
12. Yeh, J.; Lindau, I. Atomic subshell photoionization cross sections and asymmetry parameters: 1 < Z < 103. *At. Data Nucl. Data Tables* **1985**, *32*, 1–155.
13. Deslattes, R.D.; Kessler, E.G.; Indelicato, P.; de Billy, L.; Lindroth, E.; Anton, J. X-ray transition energies: New approach to a comprehensive evaluation. *Rev. Mod. Phys.* **2003**, *75*, 35–99. [CrossRef]
14. Derevianko, A.; Johnson, W.R.; Cheng, K.T. Non-dipole effects in photoelectron angular distributions for rare gas atoms. *At. Data Nucl. Data Tables* **1999**, *73*, 153–211. [CrossRef]
15. Jurvansuu, M.; Kivimäki, A.; Aksela, S. Inherent lifetime widths of Ar $2p^{-1}$, Kr $3d^{-1}$, Xe $3d^{-1}$, and Xe $4d^{-1}$ states. *Phys. Rev. A* **2001**, *64*, 012502. [CrossRef]
16. Laksman, J.; Dietrich, F.; Liu, J.; Maltezopoulos, T.; Planas, M.; Freund, W.; Gautam, R.; Kujala, N.; Francoual, S.; Grünert, J. Development of a photoelectron spectrometer for hard x-ray photon diagnostics. *Rev. Sci. Instrum.* **2022**, *93*, 115111. [CrossRef]
17. Mancuso, A.P.; Aquila, A.; Batchelor, L.; Bean, R.J.; Bielecki, J.; Borchers, G.; Doerner, K.; Giewekemeyer, K.; Graceffa, R.; Kelsey, O.D.; et al. The Single Particles, Clusters and Biomolecules and Serial Femtosecond Crystallography instrument of the European XFEL: Initial installation. *J. Synchrotron Radiat.* **2019**, *26*, 660–676. [CrossRef]
18. Galler, A.; Gawelda, W.; Biednov, M.; Bomer, C.; Britz, A.; Brockhauser, S.; Choi, T.K.; Diez, M.; Frankenberger, P.; French, M.; et al. Scientific instrument Femtosecond X-ray Experiments (FXE): Instrumentation and baseline experimental capabilities. *J. Synchrotron Radiat.* **2019**, *26*, 1432–1447. [CrossRef]
19. Laksman, J.; Buck, J.; Glaser, L.; Planas, M.; Dietrich, F.; Liu, J.; Maltezopoulos, T.; Scholz, F.; Seltmann, J.; Hartmann, G.; et al. Commissioning of a photoelectron spectrometer for soft X-ray photon diagnostics at the European XFEL. *J. Synchrotron Radiat.* **2019**, *26*, 1010–1016. [CrossRef]
20. Rörig, A.; Son, S.K.; Mazza, T.; Schmidt, P.; Baumann, T.M.; Erk, B.; Ilchen, M.; Laksman, J.; Music, V.; Pathak, S.; et al. Multiple-core-hole resonance spectroscopy with ultraintense X-ray pulses. *Nat. Commun.* **2023**, *14*, 5738. [CrossRef]
21. Kimel, A.; Zvezdin, A.; Sharma, S.; Shallcross, S.; de Sousa, N.; García-Martín, A.; Salvan, G.; Hamrle, J.; Stejskal, O.; McCord, J.; et al. The 2022 magneto-optics roadmap. *J. Phys. Appl. Phys.* **2022**, *55*, 463003. [CrossRef]
22. Ilchen, M.; Allaria, E.; Ribič, P.R.; Nuhn, H.D.; Lutman, A.; Schneidmiller, E.; Tischer, M.; Yurkov, M.; Calvi, M.; Prat, E.; et al. Opportunities for Gas-Phase Science at Short-Wavelength Free-Electron Lasers with Undulator-Based Polarization Control. *arXiv* **2023**, arXiv:2311.11519.
23. Karabekyan, S.; Abeghyan, S.; Bagha-Shanjani, M.; Block, A.; Brügger, M.; Calvi, M.; Casalbuoni, S.; Danner, S.; Decking, W.; Englisch, U.; et al. SASE3 Variable Polarization Project at the European XFEL. In Proceedings of the 12th International Particle Accelerator Conference, Campinas, Brazil, 24–28 May 2021.
24. Serkez, S.; Decking, W.; Froehlich, L.; Gerasimova, N.; Grünert, J.; Guetg, M.; Huttula, M.; Karabekyan, S.; Koch, A.; Kocharyan, V.; et al. Opportunities for Two-Color Experiments in the Soft X-ray Regime at the European XFEL. *Appl. Sci.* **2020**, *10*, 2728. [CrossRef]

25. Dahl, D.A. simion for the personal computer in reflection. *Int. J. Mass Spectrom.* **2000**, *200*, 3–25. [CrossRef]

26. Werme, L.O.; Bergmark, T.; Siegbahn, K. The High Resolution $L_{2,3}$MM and $M_{4,5}$NN Auger Spectra from Krypton and $M_{4,5}$NN and $N_{4,5}$OO Auger Spectra from Xenon. *Phys. Scr.* **1972**, *6*, 141. [CrossRef]

27. Aksela, H.; Aksela, S.; Väyrynen, J.; Thomas, T.D. $L_{2,3}M_{4,5}X$ Auger electron spectra of Br_2 and Kr: Anomalous $L_2M_{2,3}M_{4,5}$ spectra. *Phys. Rev. A* **1980**, *22*, 1116–1123. [CrossRef]

28. Levin, J.C.; Sorensen, S.L.; Crasemann, B.; Chen, M.H.; Brown, G.S. Krypton L-MM Auger spectra: New measurements and analysis. *Phys. Rev. A* **1986**, *33*, 968–976. [CrossRef]

29. Boudjemia, N.; Jänkälä, K.; Gejo, T.; Kohmura, Y.; Huttula, M.; Piancastelli, M.N.; Simon, M.; Oura, M.; Püttner, R. Experimental and theoretical study of the Kr *L*-shell Auger decay. *Phys. Rev. A* **2021**, *104*, 012804. [CrossRef]

30. Li, S.; Koulentianos, D.; Southworth, S.H.; Doumy, G.; Young, L.; Walko, D.A.; Püttner, R.; Bozek, J.D.; Céolin, D.; Verma, A.; et al. Manifestation of postcollision interaction in Krypton *LMN* Auger spectra following *K*-shell photoionization. *Phys. Rev. A* **2022**, *106*, 023110. [CrossRef]

31. Asplund, L.; Kelfve, P.; Blomster, B.; Siegbahn, H.; Siegbahn, K. Argon KLL and KLM Auger Electron Spectra. *Phys. Scr.* **1977**, *16*, 268. [CrossRef]

32. Püttner, R.; Jänkälä, K.; Kushawaha, R.K.; Marchenko, T.; Goldsztejn, G.; Travnikova, O.; Guillemin, R.; Journel, L.; Ismail, I.; Cunha de Miranda, B.; et al. Detailed assignment of normal and resonant Auger spectra of Xe near the *L* edges. *Phys. Rev. A* **2017**, *96*, 022501. [CrossRef]

33. Aksela, H.; Aksela, S.; Tulkki, J.; Åberg, T.; Bancroft, G.M.; Tan, K.H. Auger emission from the resonantly excited $1s^12s^22p^63p$ state of Ne. *Phys. Rev. A* **1989**, *39*, 3401–3405. [CrossRef] [PubMed]

34. Moddeman, W.E.; Carlson, T.A.; Krause, M.O.; Pullen, B.P.; Bull, W.E.; Schweitzer, G.K. Determination of the K—LL Auger Spectra of N_2, O_2, CO, NO, H_2O, and CO_2. *J. Chem. Phys.* **1971**, *55*, 2317–2336. [CrossRef]

35. Sorensen, S.; Miron, C.; Feifel, R.; Piancastelli, M.N.; Björneholm, O.; Svensson, S. The influence of the σ resonance on the Auger decay of core-ionized molecular nitrogen. *Chem. Phys. Lett.* **2008**, *456*, 1–6. [CrossRef]

36. Oura, M.; Gejo, T.; Nagaya, K.; Kohmura, Y.; Tamasaku, K.; Journel, L.; Piancastelli, M.N.; Simon, M. Hard x-ray photoelectron spectroscopy on heavy atoms and heavy-element containing molecules using synchrotron radiation up to 35 keV at SPring-8 undulator beamlines. *New J. Phys.* **2019**, *21*, 043015. [CrossRef]

37. Lindle, D.W.; Truesdale, C.M.; Kobrin, P.H.; Ferrett, T.A.; Heimann, P.A.; Becker, U.; Kerkhoff, H.G.; Shirley, D.A. Nitrogen K-shell photoemission and Auger emission from N2 and NO. *J. Chem. Phys.* **1984**, *81*, 5375–5378. [CrossRef]

38. Schäfers, F.; Mertins, H.-C.; Gaupp, A.; Gudat, W.; Mertin, M.; Packe, I.; Schmolla, F.; Fonzo, S.D.; Soullié, G.; Jark, W.; et al. Soft-x-ray polarimeter with multilayer optics: Complete analysis of the polarization state of light. *Appl. Opt.* **1999**, *38*, 4074. [CrossRef]

39. Hauf, S.; Heisen, B.; Aplin, S.; Beg, M.; Bergemann, M.; Bondar, V.; Boukhelef, D.; Danilevsky, C.; Ehsan, W.; Essenov, S.; et al. The Karabo distributed control system. *J. Synchrotron Radiat.* **2019**, *26*, 1448–1461. [CrossRef]

40. Ferreira de Lima, D.E.; Davtyan, A.; Laksman, J.; Gerasimova, N.; Maltezopoulos, T.; Liu, J.; Schmidt, P.; Michelat, T.; Mazza, T.; Grünert, J.; et al. Machine-learning-enhanced spectral characterization of x-ray pulses from a free electron laser. *Phys. Sci.* **2024**, *preprint*. [CrossRef]